Three-Dimensional Prediction of Lack-of-Fusion Porosity Volume Fraction and Morphology for Powder Bed Fusion Additively Manufactured Ti-6Al-4V

Vamsi Subraveti[a,†], Brodan Richter[b,†], Saikumar R. Yeratapally[c], Caglar Oskay[a,*]

[a] Department of Civil and Environmental Engineering, Vanderbilt University, Nashville, TN, USA
[b] National Aeronautics and Space Administration, Langley Research Center, Hampton, VA, USA
[c] Science and Technology Corporation, Hampton, VA, USA

[†]Both authors contributed equally to this work
[*]Corresponding author. Email: caglar.oskay@vanderbilt.edu

Abstract

Powder bed fusion (PBF) is an additive manufacturing technique that has experienced widespread growth in recent years due to various process advantages. However, defects such as porosity and the effects that porosity have on the mechanical performance remain a concern for parts manufactured using PBF. This work develops a three-dimensional framework to simulate lack-of-fusion (LoF) porosity during powder bed fusion using the voxel-based lack-of-fusion (VB-LoF) model. The framework is calibrated and validated against previously reported LoF porosity measurements and maximum equivalent pore diameter. The framework is used to study the influence of laser power, velocity, hatch spacing, and layer thickness on porosity volume fraction and morphology. Power and velocity have a linear relationship to porosity, and power has a stronger effect than velocity on changing porosity. This stronger effect of power vs. velocity contributes to high variability when relating energy density to porosity, and a modified energy density metric that weighs power heavier is shown to reduce variability. In contrast to power and velocity, hatch spacing, and layer thickness have a more complicated relationship with porosity, especially at their extrema. The influence of hatch spacing and layer thickness on pore equivalent diameter and sphericity is also explored, and four distinct morphological regimes are characterized. A LoF criteria proposed in a previous work is also confirmed. Overall, the framework offers a methodology to simulate porosity quantity and morphology and interfaces with other process-structure-property prediction techniques to support the design and development of reduced-defect powder bed fusion parts.

Keywords: Porosity, Lack-of-fusion, Powder bed fusion, Additive manufacturing, ICME, Process-structure-property relations

1. Introduction

Structurally relevant process-induced defects at the microscale, particularly those that affect mechanical properties, are a critical challenge facing powder bed fusion (PBF) additive manufacturing (AM) [1–3]. Defects frequently serve as life limiting features since they have a strong influence on the fatigue performance and other mechanical properties by forming localized stress concentrations within the microstructure of the bulk material [4, 5]. Preventing defects is therefore critical for producing high quality parts and enabling AM usage for load bearing components. As such, it is valuable to have methods to predict the occurrence of defects. Accurate prediction tools allow for accounting for the effects of defects on part performance or for modifying the design and processing conditions to mitigate defect occurrence.

The type of defect and the frequency of their occurrence during PBF depend on the specific processing conditions. Due to the rapid cooling rates and high temperature gradients present in PBF, inclusions, oxides, deleterious phases, and other microstructural inhomogeneities can be formed [2, 3]. Porosity-based defects (gas porosity, keyhole porosity, and lack-of-fusion porosity) constitute another class of PBF defects that has been widely characterized using X-ray computed-tomography (CT) or cross-section micrographs of samples [6, 7]. Absorbed gas porosity can form during solidification when the molten material has a higher solubility limit to the atmospheric gas than the solidified material [3, 8]. Residual gas porosity can be created when the powder feedstock used for the PBF build contains porosity from the original manufacturing of the powder [3, 8]. Keyhole porosity is a concern when sufficiently high powers, small beam diameters, and/or slow scanning velocities are used in the processing. In this process regime, the energy density of the laser is high enough to cause the formation of a keyhole cavity that can subsequently collapse and leave behind a pore [3, 8]. While these three types of porosity affect mechanical performance, they are generally highly spherical due to surface tension within the melt pool, which reduces potential

microstructural stress concentrations. Lack-of-fusion (LoF) porosity forms due to incomplete melting and consolidation onto previous layers or neighboring lines [3, 8]. This type of porosity occurs due to processing with either too low of power, too high of scanning velocity, too high of hatch spacing between lines, or too large of layer thickness for the material system being printed. Based on high resolution X-ray CT studies [9–11], it is evident that LoF pores have highly irregular geometry and are characterized by high aspect ratios and sharp corners. These morphological attributes of LoF pores act in concert to increase stress concentrations [12, 13], reduce the ductility of the material [13, 14], and increase the propensity of initiating fatigue cracks [14–17].

Due to the impact that LoF pores have on performance, it is critical to have capabilities to predict the morphology, location, and clustering of pores. For instance, various studies have demonstrated the initiation of fatigue cracks in the vicinity of pores located near free surfaces [18–20]. Clusters of pores can effectively reduce the fatigue strength of an AM part [21, 22]. Additionally, the shapes of process-induced pores can have a tremendous influence on the performance of an AM part. LoF pores, which have highly irregular geometries with sharp features and high aspect ratios, promote strain localizations and act as drivers for fatigue crack initiation [14, 15]. Various computational studies [17, 23, 24] have compared the strain fields in the vicinity of spherical and idealized LoF pores and demonstrated the influence of pore shape on the accumulation of strain in the vicinity of the pore. Using two independent crystal plasticity finite element (CPFE) simulations, Yeratapally et al. [24] compared the strain accumulation near an idealized LoF pore (modeled as a super-ellipsoid with sharp features) and a keyhole pore (idealized as a sphere) which occupied the same volume within the microstructure domain. It was shown that the strain near the LoF pore was significantly higher than near the keyhole pore. Cao et al. [17] demonstrated that LoF pores significantly degrade fatigue performance at high peak stresses when compared to gas/keyhole pores. Given the deleterious effects that LoF pores have on mechanical performance, it is critical to understand how to avoid LoF porosity for the usage of AM parts.

One of the most astute observations and measurable relationships for avoiding LoF pores was defined

by Tang et al. [25], who noted that the occurrence of LoF porosity can be predicted accurately knowing the melt pool geometry and processing parameters alone. Tang's LoF criterion states that the onset of LoF porosity is defined by [25]:

$$\left(\frac{L}{D}\right)^2 + \left(\frac{H}{W}\right)^2 \leq 1 \tag{1}$$

where L is the layer thickness, D is the melt pool depth, H is the hatch spacing, and W is the melt pool width. From this relationship and a constitutive equation tying processing parameters to melt pool geometry, the onset of LoF porosity can be predicted. Tang's LoF criterion was defined through observations from a two-dimensional (2D) geometric model utilizing dual half-elliptical cross-sections projected onto a 2D plane to estimate porosity. Tang characterized the influence of processing parameters on the quantity of porosity and validated the model through comparisons to experimental measurements. Several other studies have also studied the prediction of LoF porosity. Mukherjee and DebRoy implemented a numerical heat transfer and fluid flow model and proposed a non-dimensional LoF number that was linearly related to porosity volume fraction [26]. Promoppatum et al. proposed a geometric model for LoF porosity and compared to those reported in prior work [27]. Mojumder et al. utilized an active learning framework, a neural network-based symbolic regression tool, and thermo-fluid model to predict LoF porosity and proposed a normalized energy density-based expression for porosity prediction [28].

Incorporating predictions of porosity within a comprehensive integrated computational materials engineering (ICME) framework offers even greater value than the ability to predict porosity alone [29]. A wide range of simulation capabilities for PBF are in active development. For example, a variety of techniques have been developed for simulating AM microstructure evolution [30–36]. Understanding the microstructure developed during AM is important since the process frequently generates anisotropic, highly columnar grain structures and parts with a strong crystallographic texture [37–39]. The columnar grain structure and texture impact the final performance of AM components and causes anisotropic mechanical

properties [40–42]. In addition, computational microstructure evolution models can integrate with grain-level performance modeling techniques (such as the CPFE [43–46]) and enable process-structure-property (PSP) prediction frameworks for tying initial AM processing to final part performance. Incorporating porosity into these frameworks is also critical due to the impact that pores have on performance.

The present work simulates LoF pores which arise in AM processed Ti-6Al-4V using an easy-to-deploy, low computational cost method termed the voxel-based lack-of-fusion (VB-LoF) model. The VB-LoF model is built upon an open-source Potts kinetic Monte Carlo (kMC) framework that allows for AM microstructure evolution modeling and is well positioned to support PSP predictions [47–50]. This work extends the previous work by Tang et al. from 2D to three-dimensional (3D) simulations and validates their findings and their criterion for porosity onset [25]. Another contribution of the present work is in the study of porosity morphology alongside volume fraction. The influence of laser power, scanning velocity, hatch spacing, and layer thickness on the resulting porosity volume fraction is studied. The relationship between energy density and porosity is presented, and a modification is proposed. The morphology of the simulated LoF pores vs. processing conditions are also analyzed and compared to experimentally reported measurements. This porosity prediction enables the creation of higher-fidelity process structure maps in order to understand the AM parameter space and optimal parameter conditions for fully dense and near-fully dense parts.

2. Model Implementation and Validation

The present work introduces the VB-LoF modeling approach for simulating the LoF porosity during PBF AM. The model was implemented in an open-source Monte Carlo simulation framework. This section discusses the implementation of the VB-LoF model as well as the calibration and validation of the model using previously reported experimental data.

2.1. Model Implementation

2.1.1. Lack-of-Fusion Prediction Methodology

The VB-LoF model was implemented in the open-source Stochastic PARallel Particle Kinetic Simulator (SPPARKS) Monte Carlo framework developed by Sandia National Laboratories [47, 48]. The SPPARKS framework facilitates the development of new Monte Carlo applications, and includes a wide range of existing applications such as the AM module [49, 50]. In the AM module, the melt pool geometry, the scan pattern, and other variables can be readily controlled to allow for the modeling of the process. The focus of the current research is centered around calibration and in-depth examination of LoF porosity predictions within the SPPARKS framework. We note that SPPARKS is utilized to track the geometrical overlap of melt tracks for porosity prediction only. In the future, SPPARKS capabilities could be used to predict microstructure and porosity together as further discussed in Section 4.

The VB-LoF approach tracks the geometrical overlap of the melt tracks on a voxelated, 3D cubic lattice to identify lattice sites that have not been melted. Each lattice site, i, has a marker q_i to distinguish between the unmelted ($q_i = 1$) and melted ($q_i \neq 1$) state. When the computational domain is initialized, the markers for all lattice sites are set to 1 to indicate that the initial state of the material is unmelted powder. During the simulation, the melt pool scans across the domain based on the input scan path. If a site is ever within the melt pool, the marker of the site permanently switches away from 1 to indicate that it has been melted. This allows for the identification of lattice sites that were not melted over the course of the simulation. The simplicity of this approach, in conjunction with the open-source AM module in SPPARKS, allows for the simulation of a range of PBF processing scenarios.

The simulations were performed with a domain size of 100×100×100 voxels. Edge effects were determined to be negligible on porosity volume fraction when comparing a 200×200×200 voxels sized samples with their smaller counterparts. The defect morphology validation study used a larger 200×200×200 domain size with the same voxel resolution due to the need to measure porosity size in

addition to the porosity volume fraction. The spatial resolution of the simulations was set to 3 μm per lattice site to simulate large domains with a relatively low computational cost due to the quantity of simulations being performed. The samples were run on 64-processor compute nodes (Intel, Xeon Gold 6130 CPU). Each sample took on the order of minutes to run, depending on scanning velocity. In addition to being straightforward to implement, the VB-LoF model is advantageous in its low computational cost that allows a wide design space to be surveyed. For the present work, over 1400 3D simulations were run.

After the simulation, unmelted sites were filtered from the rest of the simulation domain to extract pore morphology data. The relationship between porosity and the microstructure was not characterized in this current work since calibrating and validating microstructure prediction represents a substantial effort and is on-going. The porosity was extracted, segmented, and analyzed using DREAM.3D [51]. From the segmented pores, the maximum defect diameter, equivalent diameter, and sphericity were calculated. The maximum defect diameter was defined as the longest axis length of the pore. The equivalent diameter was defined as the diameter of a sphere with the same volume as the pore. The sphericity (Ψ) was calculated with the volume of the pore (V_p) and surface area of the pore (A_p) using [52]:

$$\Psi = \frac{\pi^{1/3}\left(6V_p\right)^{2/3}}{A_p} \tag{2}$$

A sphericity of 1 reflects a perfect sphere and is the maximum sphericity value a pore can take, while a sphericity of 0 is the lowest possible sphericity value and represents a sample with either an infinitely large surface area or infinitesimally small volume.

2.1.2. Melt Pool Geometry and Size

The prediction of LoF porosity is strongly dependent on the melt pool geometry. The melt pool geometry in the AM module was modified to resemble experimentally imaged Ti-6Al-4V melt pools, as

shown in Figure 1. The experimental image was taken using visible bright field optical microscopy (Leica, DMi8 C[1]).

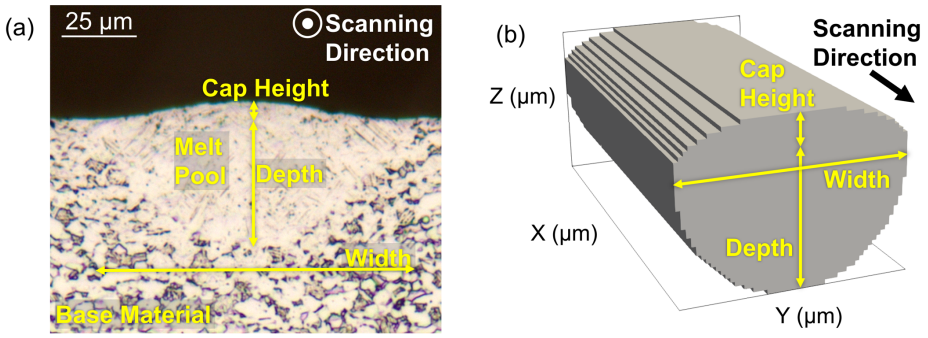

Figure 1. Examples of an (a) experimentally imaged melt pool compared to a (b) laser scan track with augmented melt pool in SPPARKS. The experimentally imaged melt pool had a laser power of 100W and scan velocity 500 mm/s.

Dilip et al. imaged cross-sections of melt pools and heat affected zones produced by various laser power and velocity combinations for bare-plate Ti-6Al-4V [53]. When the melt pool is in the conduction mode (*i.e.,* low power and/or high scanning velocity), the melt pool cross section is bi-elliptical (Figure 1(a)) [53]. Capturing the melt pool geometry accurately contributes to the reliability of LoF volume fraction and morphology predictions. Tang et al. demonstrated that the ratio of the cap height to the total melt pool depth had a negligible role in the total simulated porosity [25]; however, the shape of the cap will influence the morphology of the LoF pores. To address the potential impact of cap shape on the defect morphology, the melt pool constructor in the AM module was augmented with the melt pool cap geometry. The addition of the melt pool cap to the melt pool depth captures the bi-elliptical nature of the melt pool when compared to experimental images (Figure 1(a)). Conduction mode melt pool cross sections from Dilip et al. [53] were analyzed using image analysis software (ImageJ, [54]) to estimate the melt pool cap height. Based on these measurements, the melt pool cap was set to 15% of the melt pool depth.

[1] Specific vendor and manufacturer names are explicitly mentioned only to accurately describe the test hardware. The use of vendor and manufacturer names does not imply an endorsement by the U.S. Government nor does it imply that the specified equipment is the best available

The melt pool geometry was predicted from an augmented version of the Rosenthal equation that was calibrated using pre-existing data in the literature for melt pool width and depth as a function of processing parameters. The Rosenthal equation, which is the solution to a point heat source in a semi-infinite medium, has been used to approximate melt pool geometry in a large number of AM and welding publications (e.g., [27, 55, 56]). Tang et al. [25] presented an approximation to the Rosenthal equation to allow for calculation of the width (W) of the melt pool:

$$AP \approx \pi k(T_m - T_0)W + e\pi\rho c(T_m - T_0)VW^2/8 \quad (3)$$

where T_0 is the initial temperature of the substrate, T_m is the melting temperature of the material, A is the absorption coefficient of the surface to the laser light, P is the laser power, V is the laser scanning velocity, k is the thermal conductivity of the material, ρ is the density, c is the specific heat, e is Euler's number, and W is the width of the melt pool. This approximation was used in this work to estimate the melt pool width vs. processing conditions. The thermophysical values used in this work for modeling the melt pool width and depth are given in Table 1.

Table 1. Thermophysical values used in the simulations for AM Ti-6Al-4V specimens [25].

Property	Symbol	Value	Units
Thermal conductivity	k	6.7	(W/m-K)
Density	ρ	4430	(kg/m^3)
Heat capacity	c	526	(J/kg-K)
Melting temperature	T_m	1913	(K)
Ambient temperature	T_0	303	(J/kg-K)

Energy density metrics are also frequently used in the context of AM to condense the processing parameters into a single metric. The most frequently used energy density metric in the context of AM is the volumetric energy density (VED), which is defined as [1, 57]:

$$VED = \frac{P}{VHL} \tag{4}$$

where H and L are the hatch spacing, and layer thickness, respectively. The melt pool geometry is hemispherical at lower VED values and transitions into a non-hemispherical, keyhole-like shape at higher VED values; these two modes are commonly referred to as the conduction mode and the keyhole mode, respectively [58]. To better estimate the non-hemispherical melt pool geometry outside of the conduction mode and near the keyhole mode transition, the calculated depth was augmented with experimental data. To account for the under-prediction of melt pool depth at higher energy densities, we consider the melt pool aspect ratio, a, (melt pool depth/melt pool width) to be a function of V and P. A quadratic polynomial surface (Eq. 5) for the melt pool aspect ratio with fit constants (Table 2) was fitted using least squares regression to experimental data gathered by Dilip et al. [53].

$$a(P,V) = C_0 + C_1P + C_2V + C_3PV + C_4P^2 + C_5V^2 \tag{5}$$

Table 2. Constants used in the polynomial surface of aspect ratio vs. power and velocity (Eq. 5)

Constant	Value	Units
C_0	2.523×10^{-1}	
C_1	4.470×10^{-3}	(1/W)
C_2	-4.979×10^{-4}	(s/mm)
C_3	-2.314×10^{-6}	(s/mm-W)
C_4	3.938×10^{-6}	($1/W^2$)
C_5	2.902×10^{-7}	(s^2/mm^2)

The quadratic polynomial surface had a coefficient of determination (R-squared/R^2) of 0.981 and adjusted coefficient of determination of 0.969 with the experimental data. An R^2 value of 1 indicates a perfect fit, which demonstrates that the quadratic polynomial surface has a good fit to the experimental data. The comparison of the fitted response surface and the experimental measurements in the power-velocity space is shown in Figure 2. The polynomial surface was then used to estimate the melt pool depth

based on the melt pool width value predicted by Eq. 3 (*i.e.*, $D = W \times a(P,V)$). This approach maintains an elliptical melt pool within the keyhole mode and does not fully capture the actual keyhole melt pool shape. However, in the present work, the processing near the keyhole mode showed LoF porosity below the threshold value of 0.1%. At this low LoF porosity regime, the effect of shape deviations is likely insignificant.

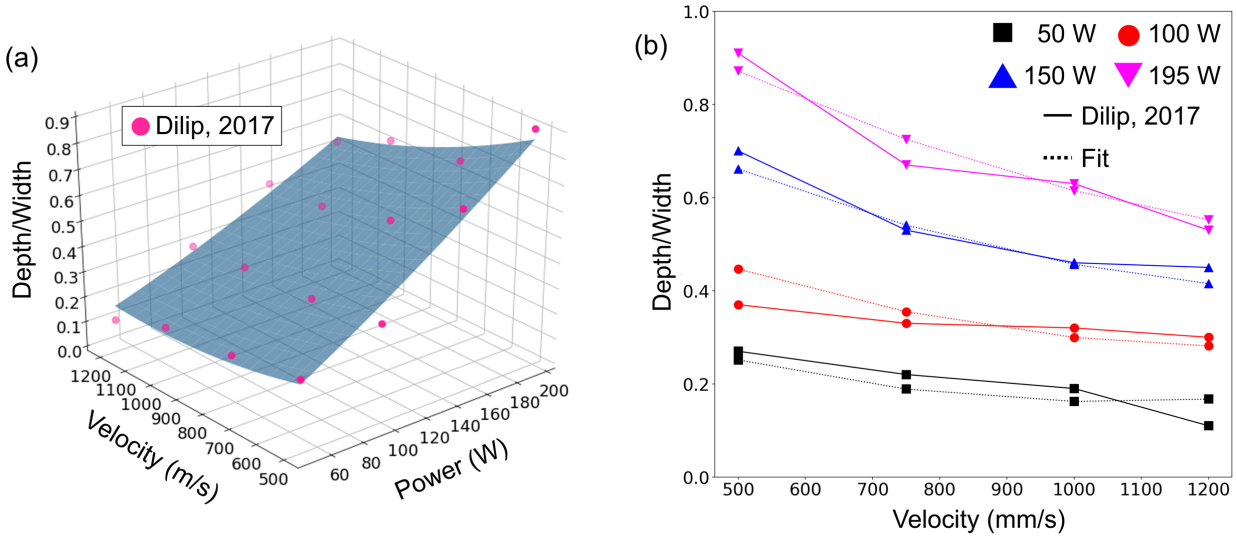

Figure 2. (a) Plot of $a(\mathrm{P},\mathrm{V})$ and data from Dilip et al. [53] showing melt pool aspect ratio, taken to be depth/width; (b) $a(\mathrm{P},\mathrm{V})$ evaluated at each (P, V) from Dilip et al. [53].

2.2. Model Calibration and Validation

The porosity volume fractions from the LoF model were calibrated and validated by comparing the predicted values to experimentally reported values. The model was further validated by comparing the predicted defect morphology to experimentally reported morphology.

2.2.1. Volume Fraction

One of the primary parameters in the Rosenthal equation approximation for melt pool width (Eq. 3) is absorptivity, which has been shown in the literature to vary significantly for Ti-6Al-4V [59, 60]. In previous studies using the Rosenthal equation for melt pool geometry approximation, the absorptivity of Ti-6Al-4V was estimated at 0.38 [61] and 0.48 [56]; both of these studies used absorptivity measurements of bare-

plate Ti-6Al-4V. Studies measuring the absorptivity of powder Ti-6Al-4V in situ have reported a maximum absorptivity of approximately 0.74 [59, 60]. Other absorptivity estimation approaches, such as using ray tracing and a variety of powder packing schemes, have also reported that bare-plate and powder absorptivity differ significantly [60]. It is apparent that the absorptivity of powder Ti-6Al-4V has significant uncertainty, and therefore contributes to the uncertainty of the melt pool geometry prediction using the Rosenthal equation.

The absorptivity was used to calibrate the LoF model. To test that the model captured melt pool geometry in the conduction mode (*i.e.,* a semicircular cross-section geometry) as well as in the keyhole transition (*i.e.,* a non-semicircular cross-section geometry), the absorptivity was set to 0.38 and melt pool geometry was computed from the modified Rosenthal equation. These predictions were plotted against experimentally measured melt pool geometry (Figure 3) [53]. Melt pool width predictions from the Rosenthal equation agreed with experimental results, except for the lowest power setting. The experiments reported balling at this power setting, a phenomenon that occurs when the energy density is not high enough to form a well consolidated and smooth melt pool. The melt pool depth predictions with the dynamic aspect ratio term were also in good agreement with the experimental values.

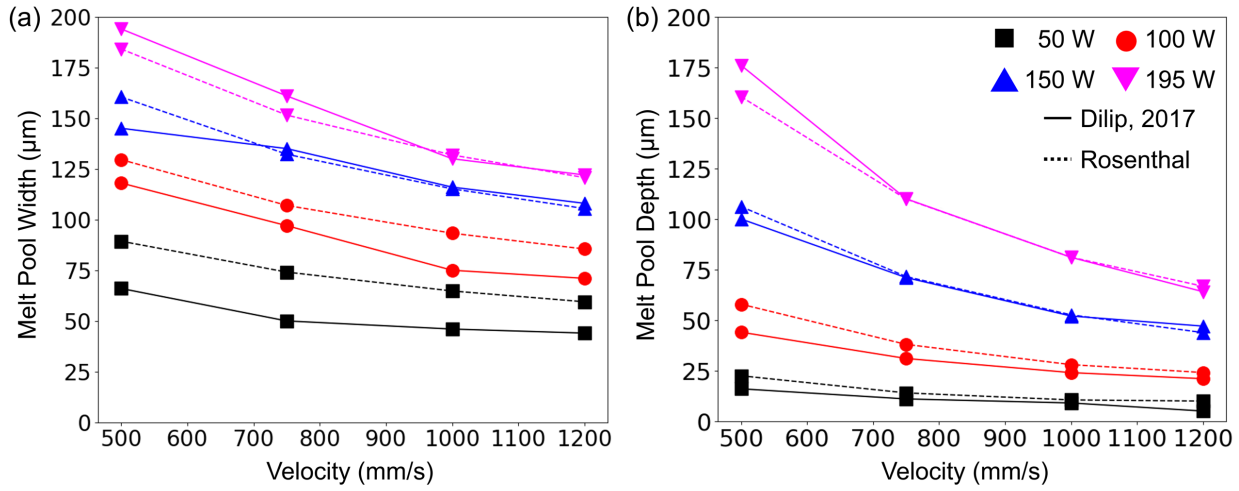

Figure 3. Melt pool width (a) and melt pool depth (b) vs. power and velocity comparing experimental (solid) and predicted (dashed) values [53]. Melt pool geometry was estimated for bare-plate conditions (*i.e.,* $A = 0.38$). Both plots share the legend in (b).

The calibration of the model for PBF of Ti-6Al-4V was performed by modifying the absorptivity between 0.38 (reported bare-plate value) to 0.74 (reported powder value) – and therefore altering the melt pool geometry – until the porosity predictions from the model matched with reported porosity in two different calibration experiments [56, 62]. Data used for calibration had a range of powers and constant laser velocity (1200 mm/s), hatch spacing (140 μm), layer thickness (30 μm) and layer rotation (67°) values for both studies. The calibration experiments also reported keyhole porosity at high energy densities (Fig. 4), which cannot be predicted by the proposed model. The effect of keyhole porosity is observed at a critical point in the porosity trendline (between 40 J/mm^3 and 50 J/mm^3 in Fig. 4), beyond which the experimental porosity volume fraction shows a positive slope. At energy densities less than the keyhole transition zone, LoF porosity was reported to be the largest contributor to total porosity [56, 62]. For the purposes of the model, high and low porosity extremes were not considered. A central range of functional porosity (0.1% – 5% volume fraction) was considered for calibration and validation. The 0.1% porosity threshold was chosen since small porosity values will be strongly influenced by noise and the specific segmentation technique used to distinguish between noise and porosity [63].

The predicted variation of porosity as a function of energy density in the LoF regime using four absorptivity values ranging between 0.45 and 0.70 is shown in Figure 4(a). An absorptivity of 0.61 was found to minimize the discrepancy between measured and the simulated porosities and was used as the calibrated value in the subsequent simulations. Both experimental studies used for calibration employed the same machine model and manufacturer (EOS GmbH, M290). The discrepancy in porosity between the two sets of experiments at higher energy densities is believed to be due to differences in how the porosity was classified and the sample measurement size and region. The porosity size range 20 μm – 40 μm was not considered in the post-process porosity classification by Gordon et al. [56]. In addition, the entire 5 mm × 5 mm × 5 mm part was scanned using micro-CT by du Plessis et al. [62], as opposed to only the top 1.5 mm^3 (dimensions approximately 1 mm × 9 mm × 0.167 mm) by Gordon et al. [56].

The calibrated model was then validated against additional data from du Plessis et al. that was not used for calibration [62]. This data had a range of powers and constant velocity (800 mm/s), constant hatch spacing (140 µm), constant layer thickness (30 µm), and constant layer rotation (67°) values. The validation data therefore substantially differs from the calibration data in velocity, but all the other parameters are the same. The different velocities will cause the simulated melt pool widths and depths to differ even at similar energy density values due to the respective impact power vs. velocity has on the melt pool geometry (Figure 3). The comparison of model predictions and validation data is shown in Figure 4(b).

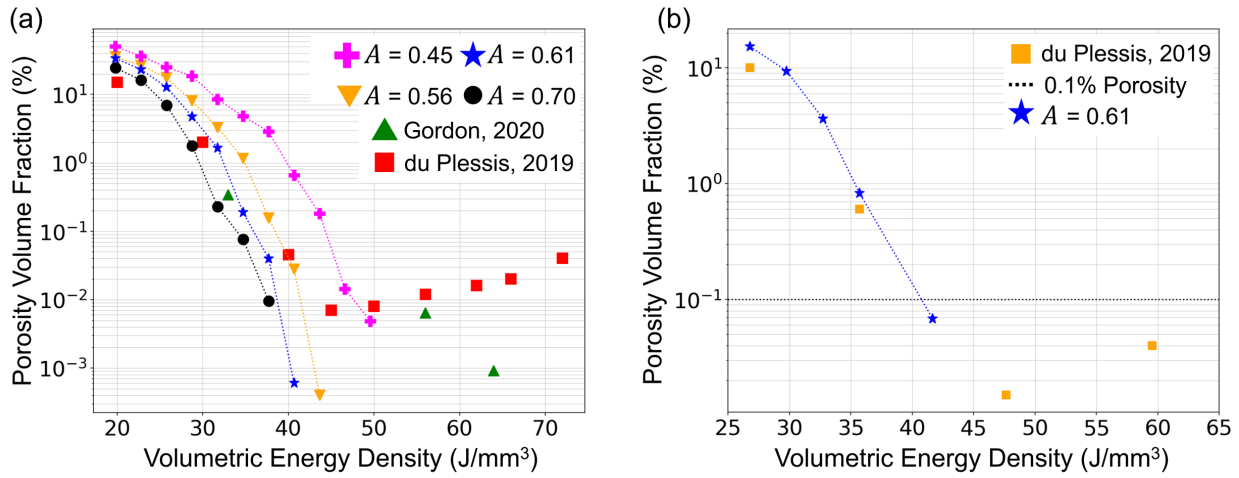

Figure 4. (a) Calibration and (b) validation of the LoF model based on experimental data [56, 62].

The two curves differ since they use a different laser scanning velocity (1200 mm/s vs. 800 mm/s)

The LoF model has good accuracy at porosity volume fractions between 0.1% – 5% when an absorptivity of 0.61 is used. Above the 0.05% – 1% range, the model tends to overestimate the porosity volume fraction, while below it underestimates the porosity. Other absorptivity values work better at high and low VED values – however, an absorptivity of 0.61 worked well at porosity volume fractions of interest for practical usage. Also note that the predicted porosity volume fraction drops to zero percent at energy densities between 40 J/mm^3 and 50 J/mm^3 while the experimental data observes an increase in porosity due to the occurrence of keyhole porosity.

Another point of consideration is how powder may interact with a LoF pore. The powder and LoF pores may have a similar size scale. Large pores may contain unmelted powder, while small pores may result from the void between partially melted powder and the melt pool [7,8]. It is not well described how the post-processing of the CT data used for calibrating and validating the model may have accounted for porosity that was partially filled with powder. For example, the CT scans used by du Plessis et al. had a voxel resolution of 10 μm and could determine pores with sizes of 2×2×2 voxels and greater [62]. The powder used in PBF often has diameters ranging between 10 μm and 60 μm [64], which is sufficiently small that a detectable pore could be filled with powder and impact the detectability of the pore. Tang et al. accounted for powder-influenced porosity by scaling the apparent density based on the packing density of the powder [25]. This can be implemented in the present work through Eq. 6, where the simulated porosity volume fraction (Vol_{LoF}) is scaled by the packing density of the powder ($\rho_{packing}$) to calculate an adjusted porosity volume fraction (Vol_{adj})

$$Vol_{adj} = Vol_{LoF}\left(1 - \rho_{packing}\right) \tag{6}$$

If a packing density of 60% for Ti-6Al-4V is used [64], the adjusted volume fraction can be calculated. The adjusted porosity volume fractions compared to the original porosity volume fractions and calibration and validation data are shown in Figure 5.

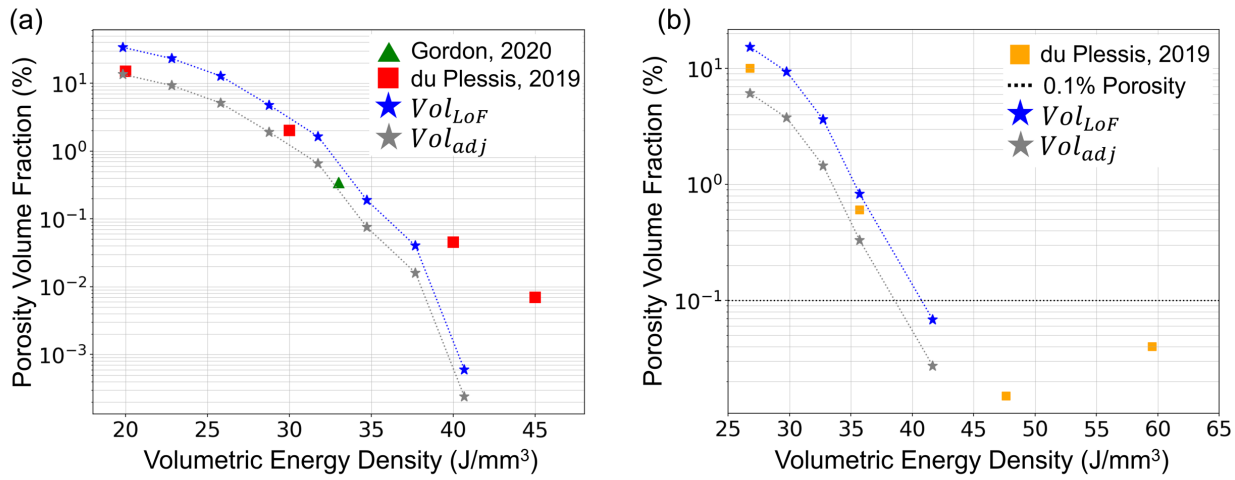

Figure 5. Comparisons of the adjusted porosity volume fraction vs. original porosity volume fractions for the (a) calibration and (b) validation data.

The adjusted porosity volume fraction generally underestimates the experimental porosity volume fraction. Uncertainty around how the CT analysis was calibrated may have accounted for partially filled porosity, thus the figures found in the rest of the present work will consistently refer to Vol_{LoF}. However, they can be easily adjusted using Eq. 6.

2.2.2. Defect Morphology

One of the primary advantages of the VB-LoF model is that it allows for direct morphological comparisons between defects predicted by the model and defects observed in experiments. Montalbano et al. [65] reported the effects of energy density on defect volume fraction and maximum defect diameter on Ti-6Al-4V specimens. The VB-LoF model was used to compare simulated maximum defect diameters to those found experimentally. The comparison between the experimentally observed defect diameters and the numerical simulations is shown in Figure 6. The experimentally built samples LF1 and LF2 had a hatch spacing of 140 µm, a layer thickness of 30 µm, and a velocity of 1200 mm/s. LF1 was built with laser power 160 W, and LF2 was built with 130 W [65]. The numerical simulations employed the calibrated absorptivity value provided in the previous section.

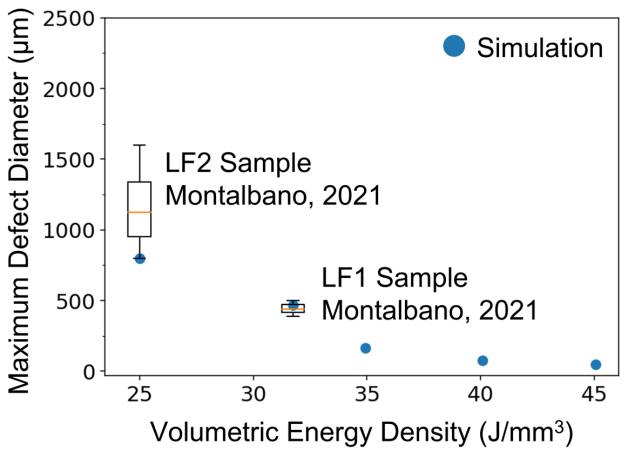

Figure 6. Maximum defect diameter vs. energy density plot. The blue points show the maximum diameter in the simulated sample corresponding to the energy density input as reported in Montalbano et al. 2021 [65]. Note that for low energy densities outside of the functional prediction range (< 30 J/mm^3), LoF porosity presents as interconnected structures spanning the entirety of the simulation domain.

The LoF model predicted a maximum defect diameter for LF1 within the reported range from Montalbano et al. [65]. The maximum defect diameter was then predicted for samples at higher energy densities of interest (30 J/mm^3 - 45 J/mm^3) before complete melting occurred. At energy densities lower than this range (including the LF2 case), LoF structures were interconnected throughout the entirety of the domain, implying a true pore size larger than the simulation domain. However, the LoF prediction methodology does not model fluid effects such as surface tension which will affect defect morphology [66]. Energy densities higher than this range presented little LoF porosity, indicating complete melting. The 3D and 2D LoF porosity structure generated for LF1 is shown in Figure 7.

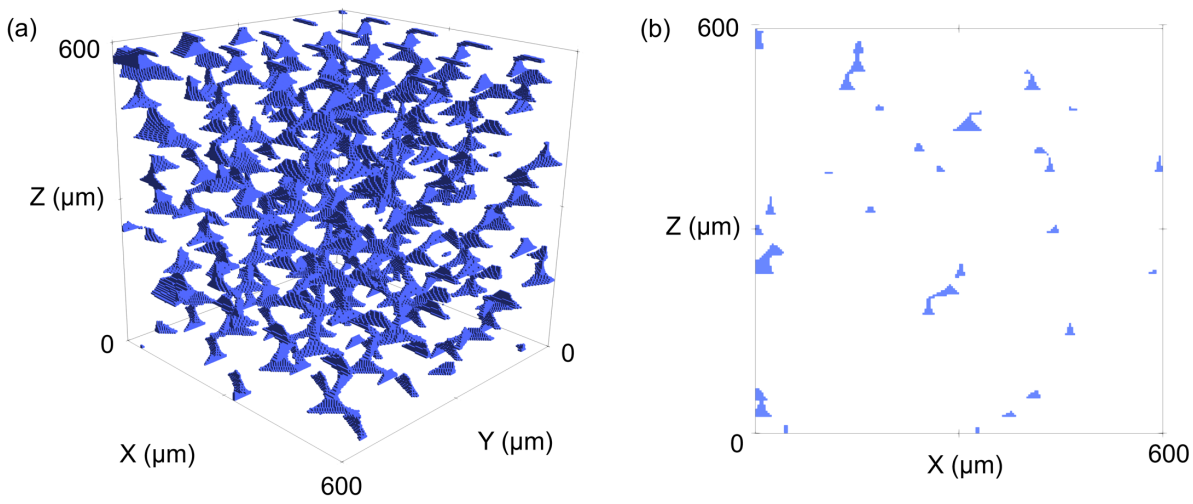

Figure 7. Simulated LoF pores that mimic sample LF1 from Montalbano et al. [65] shown in (a) 3D and in a (b) 2D cross-section of the 3D domain taken at the midpoint of the Y-axis at a position of 300 μm.

While the 3D structure shown in Figure 7(a) seems to show a substantial amount of porosity, the 2D cross-section resembles a polished sample cross-section with porosity. The LF1 simulations shown in Figure 7 had a simulated porosity volume fraction of 3.43% porosity and an adjusted porosity volume fraction of 1.37% vs. a reported porosity volume fraction of approximately 1% [65].

3. Model Predictions and Discussion

The validated VB-LoF model was used to predict LoF porosity with a wide range of processing conditions to create maps across the process space (process maps). These process maps were used to observe porosity trends across the process-parameter space and relate porosity to AM build parameters such as laser power and scanning velocity. Process maps generated by sampling the model parameters and simulating using the validated LoF model could provide build guidelines, help process parameter selection, and provide porosity predictions across a wider domain in the process space than is conventionally accessible through experimental build methods.

The two process parameter spaces that were sampled were the power-velocity space (PV space) and the scan pattern parameter space (LH space). To populate the PV space, the scan pattern parameters were

held constant at a hatch spacing of 140 µm and a layer thickness of 30 µm while the power and velocity were varied. For the LH space, the power was held constant at 280 W, and the velocity was held at 1200 mm/s, while the hatch spacing and layer thickness were varied. For the process parameter samples in both spaces, the layer rotation was held constant at 67°. These choices for constant values were based on the processing conditions used in previous experimental studies [56].

3.1. Influence of Laser Power and Scanning Velocity

The PV space was populated by using random sampling of powers between 80 W - 200 W and velocities between 600 mm/s - 1300 mm/s. A small number of these samples are located near the keyhole transition regime, where the true shape of the melt pool deviates from the bi-elliptical conduction-mode shape. The shape deviations likely had no impact on the prediction of LoF porosity near this regime, as the volume fractions were below the 0.1% porosity threshold. A total of 975 samples were used to generate the contour plot of porosity shown in Figure 8. The volume fraction of porosity across the PV space is shown in Figure 8.

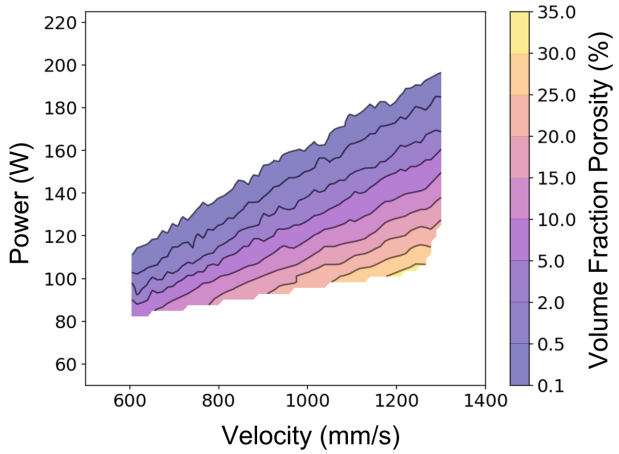

Figure 8. PV space showing porosity contours ranging from 0.1% to 35%.

The simulated LoF porosity follows a linear trend within the sampled PV space (Figure 8). When the linear trend is normalized by scaling the maximum and minimum power and velocity between 0 and 1, the following relationship for the porosity volume fraction can be defined for the linear region as:

$$Vol_{LoF} = C_P\tilde{P} + C_V\tilde{V} + C_I \quad (7)$$

where C_P and C_V are scaling constants for the normalized power ($\tilde{P}$) and normalized velocity ($\tilde{V}$) and equal to -47.1 and 37.6, respectively, and C_I is an intercept term equal to 7.8. This relationship has an adjusted coefficient of determination value of 0.95. The normalization allows for direct comparisons of the effect of the power and velocity through the scaling constants. The absolute value of C_P is approximately 25% larger than C_V, indicating that changes in power are a stronger contributor to the final LoF porosity than equivalent changes in velocity. The relationship between porosity volume fraction and VED was also studied, which is shown in Figure 9.

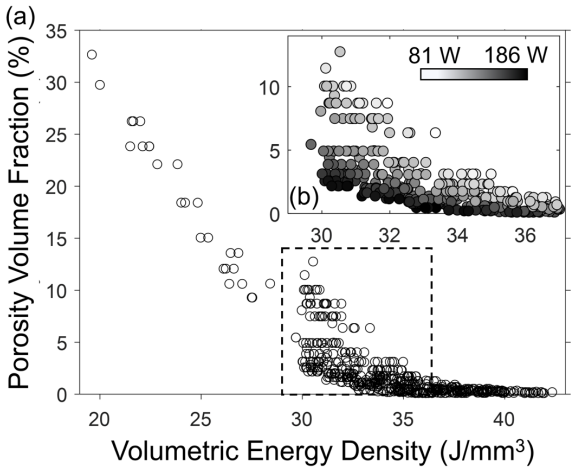

Figure 9. Impact of VED on the resulting LoF porosity across the (a) entire VED space and across (b) a subregion of high VED values shown in the dotted box.

A trend was found between a decreased VED and an increased porosity. This trend between porosity and VED is well known [1, 67], and this result demonstrates that the VB-LoF model captures the same behavior. However, there is also high variance in the data at VED values around than 31 J/mm^3. These values are shown in more detail in the inset plot in Figure 9(b), where the power values are indicated based on the coloring of the individual data points. For a set VED value, the power decreases from a high to a low value as the porosity volume fraction increases. Maintaining an equivalent VED requires changing the velocity varying an equal amount. The high variance in the relationship between VED and porosity at VED

values greater than 29 J/mm^3 can be explained by the difference in the normalized coefficients of the linear fit given by Eq. 7. The VED weighs changes in power and velocity equally – a equivalent increase or decrease in both power and velocity will give an equivalent energy density, even though the impact of power is approximately 25% higher. The variance in the relationship between energy density and porosity can be reduced by instead considering a modified energy density (MED) that weighs power stronger than velocity by raising power to the 5/4th power. The relationship between porosity volume fraction and MED is shown in Figure 10.

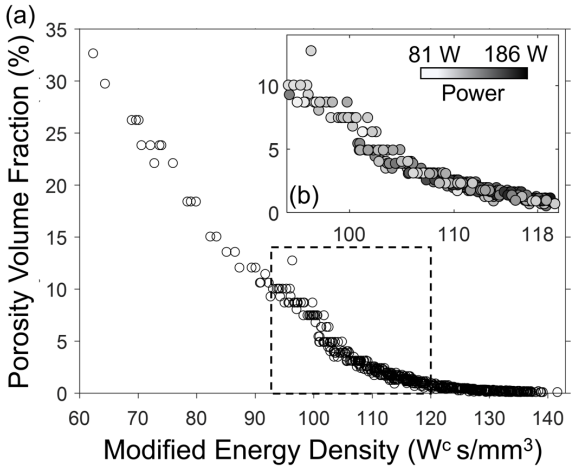

Figure 10. Impact of MED on the resulting LoF porosity across the (a) entire MED space and across (b) a subregion of high MED values shown in the dotted box.

This stronger weighting of power in the *MED* reduces the variability in the data and allows for estimating a more accurate porosity based on the *MED*. The reason for weighing power more can also be understood by looking at how the power vs. velocity impact the melt pool depth and width (Figure 3). Increasing the power has a stronger effect on the melt pool geometry than decreasing velocity when both are changed a comparative amount. However, the 5/4th exponent should not be considered a universal constant as the value of the exponent likely depends on the thermophysical properties of the material and other build parameters such as the layer thickness and hatch spacing that are studied in the following section.

3.2. Influence of Layer Thickness and Hatch Spacing

The LH space was populated by sampling the ratio between the layer thickness and effective depth (L/D_e) and the ratio between the hatch spacing and melt pool width (H/W) at regular intervals. The effective depth (D_e) was defined to be the sum of the melt pool depth calculated using Eq. 3 and Eq. 5 and the melt pool cap. The effective depth is equal to the total melt pool geometry component in the build direction (the Z direction in Figure 1). Using the melt pool width and effective depth, L/D_e and H/W were sampled within the ranges of 0.1–1.25 and 0.1–1.4, respectively. These bounds were used to limit the number of simulations that need to be performed to generate the process map. For example, if a layer thickness value is close to 0 µm, then the build time for the part would be high and is likely not feasible due to the size range of the powder used in powder bed fusion. Therefore, such a run was not simulated. Tang's LoF criterion (Eq. 1) predicts 0% porosity for process parameters satisfying the inequality; however, some samples with process parameters satisfying Eq. 1 presented with nonzero porosity close to L/D_e= 1. These outliers were determined to result from the discretization of the elliptical shape of the cap and the bottom of the melt pool onto the voxel-base lattice of the simulation. When L is close to D_e, the discretization of the elliptical shape of the melt pool sometimes results in porosity.

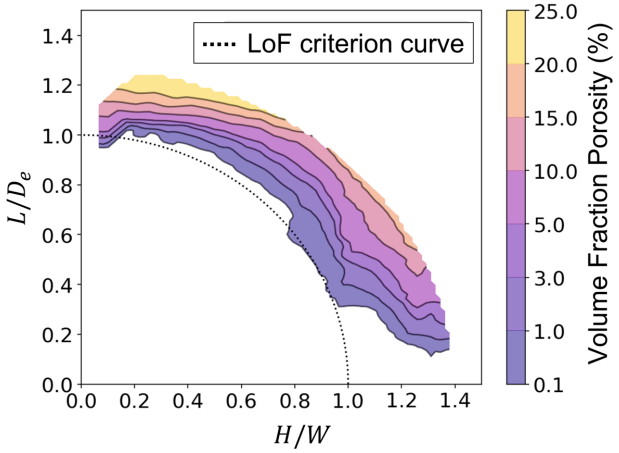

Figure 11. LH space showing porosity contours ranging from 0.1% to 25%.

The contour map of LoF pore volume fraction in the LH space around Tang's LoF criterion curve, given in Eq. 1, is shown in Figure 11. A total of 448 samples were used to generate the contour plot of

porosity in Figure 11. The porosity threshold predictions of the proposed model are consistent with the previously derived threshold for LoF porosity. The inverse-sigmoidal trend of the predicted contours also matches well with porosity contours predicted by Tang for AlSi10Mg [68]. The upper left portion of the LH space where L/D_e is greater or equal to 1 is also the region of the most rapid increase in porosity content. In contrast, the lower right portion of this space where H/W is greater or equal to 1 is the region of the slowest increase in porosity content. This is since a small L/D_e can mitigate the effects of a large H/W through additional melting of previous layers due to deep melt pools and scan orientation rotation between layers. In contrast, decreasing H/W does not eliminate porosity that exists when L/D_e is greater than 1.

3.3. Pore Morphology

The LoF prediction methodology was also used to analyze the pore morphology across the LH space. The power was held constant at 280 W, and velocity was held constant at 1200 mm/s. Like the volume fraction prediction, L/D_e and H/W were sampled at regular intervals, and the measured volume-weighted mean equivalent diameters are shown in Figure 12.

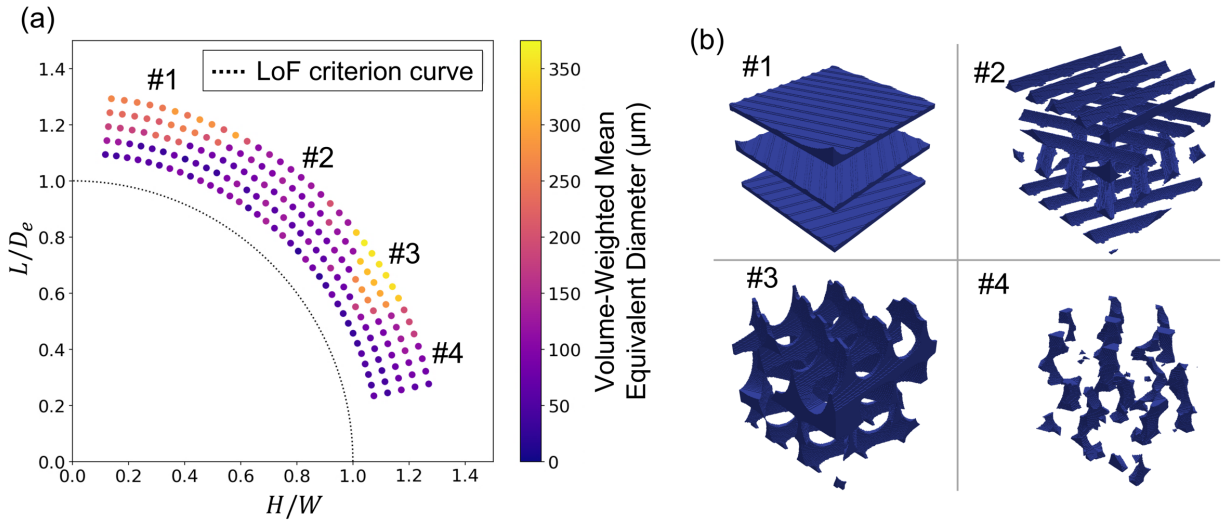

Figure 12. LH space showing (a) volume-weighted mean equivalent diameter of the pores in each sample, and (b) characteristic porosity within region shown in (a).

There are four distinct regions that can be observed in Figure 12(a) and the corresponding porosity within those four regions are shown in Figure 12(b). The upper left portion, labeled #1, contains pores that are characteristic of a large layer thickness and small hatch spacing. The layer thickness is large enough that a continuous void between layers is seen which causes a large overall porosity volume fraction (Figure 11). The middle-left portion, labeled #2, has a larger hatch spacing and smaller layer thickness than #1. The porosity in this region is defined by large tracks between sequential melt tracks. The layer thickness is small enough that there is no longer a continuous void between layers. The middle-right portion, labeled #3, is the region with the largest pores. In this region, the hatch spacing and layer thickness combination cause a continuous web of interconnected porosity. The final region in the lower right, #4, has a small layer thickness and large hatch spacing. This leads to sporadic, columnar voids and a lower overall porosity (Figure 11). While the examples of porosity shown in Figure 12(b) are exaggerations vs. those observed in practice, the examples suggest that LoF porosity has regimes within itself where the relational characteristic between pores depends on an interrelation effect between hatch spacing, layer thickness, melt pool depth, and melt pool width.

In addition to the mean equivalent diameter, the volume-weighted mean sphericity was calculated to characterize the impact of hatch spacing and layer thickness on the porosity morphology. The characterized sphericity and two samples exhibiting similar porosity volume fractions but different morphologies are presented in Figure 13.

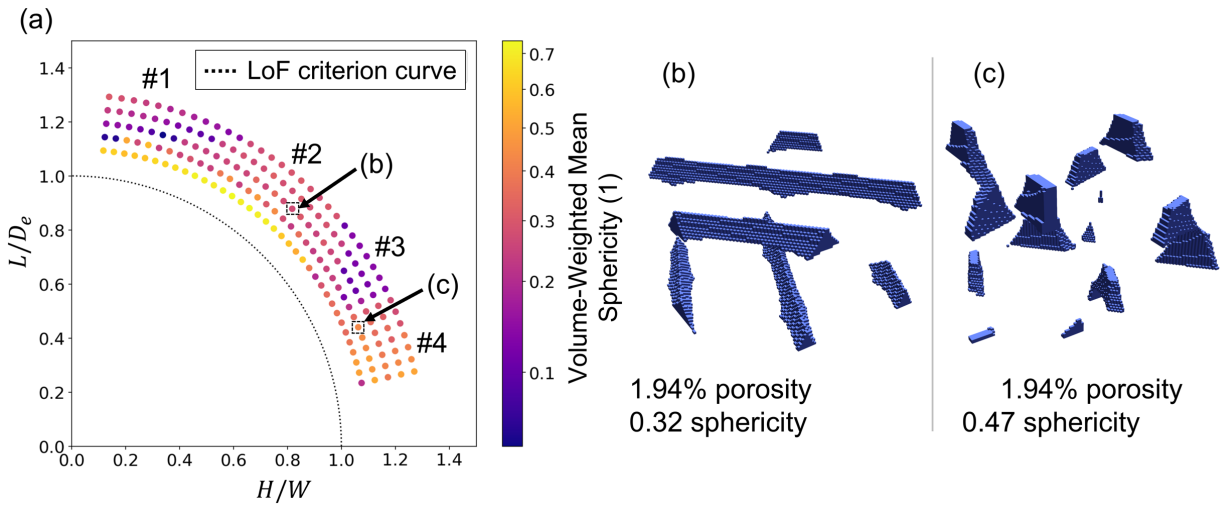

Figure 13. LH space showing (a) volume-weighted mean sphericity of the pores in each sample, and (b,c) two samples that exhibit similar porosity fractions but different morphologies and sphericities.

The four regions seen in the volume-weighted mean equivalent diameter measurements (Figure 12) can been seen in the sphericity. The pores in region #4 have higher sphericity alongside a lower equivalent diameter. The pores in region #3 in general have the lowest sphericity alongside their high equivalent diameter. Region #2, which were long pores located between melt tracks, had low equivalent diameters and moderate sphericities. An example comparing two samples from regions #2 and regions #4 are shown in Figure 13(b) and 13(c). These two samples had similar porosity volume fractions but different sphericities and pore morphologies.

4. Limitations and Extensibility

The present framework has several limitations that could be relaxed in later iterations of the VB-LoF model. The first limitation is in using the Rosenthal equation to predict melt pool morphology. Due to the equation being the solution to a point heat source, the predicted melt pool depth will be half the melt pool width. While the change in the melt pool depth across the domain space was accounted for using the fit discussed in Figure 2, the adjusted melt pool depth will still be elliptical and not necessarily reflective of the keyhole-like shape that occurs at high energy densities. The present model also did not simulate laser turn-around regions, contouring regions, or the balling phenomena which occurs at high scanning velocities.

Additionally, melt pool dynamics were not explicitly modeled, which would affect pore morphology. These limitations could be relaxed through using higher-fidelity models such as computational fluid dynamic (CFD) simulations of PBF that can accurately capture transient melt pool evolution. However, CFD simulations would increase the required computational demand and limit the design space that can be explored using the model. Another limitation is that the model in the current work does not resolve individual powder particles, and instead considers each powder layer as bulk material. Not resolving the powder could affect the volume fraction, equivalent diameter, and sphericity of the predicted porosity. To rectify this, the powder layer could be explicitly modeled using techniques such as the discrete element method (DEM) and resolving the individual powder particles at the cost of increased computational resources and complexity.

The VB-LoF model could be extended in various ways. For example, the methodology supports simulating microstructure evolution alongside the porosity prediction. However, the calibration and validation of microstructure evolution parameters requires a dedicated study with numerous experimental conditions within the LoF build regime. This work focused on calibrating and validating the porosity prediction component. The VB-LoF could also incorporate stochastic melt pool geometry to model how local fluctuations in melt pool geometry may impact the porosity volume fraction and defect morphology. This work also has extensibility in supporting PSP predictions for PBF in a ICME framework. The results described within this paper further the development of the simultaneous prediction of porosity and microstructure, form the foundation for characterizing uncertainty and sensitivities due to the presence of defects in microstructures [69–71] and offers a methodology for generating pseudo-microstructures for incorporation into multiscale structural performance modeling techniques [72–74].

5. Conclusions

The present work developed, calibrated, and validated an easy-to-deploy, low computational cost VB-LoF model to simulate the volume fraction and morphology of LoF porosity during PBF AM. An analytical

model of the melt pool geometry during PBF was calibrated to experimental data based on absorptivity and a depth-scaling factor. The predicted melt pool geometry was used in the VB-LoF model that was calibrated and validated through non-blind and blind comparisons with experimental measurements of LoF porosity volume fractions. The validated LoF porosity prediction was then used to determine the impact of laser power and scanning velocity on the resulting porosity predictions. It was found that LoF porosity had a linear relationship with velocity and power, and power was found to have a stronger effect than velocity on porosity. The effect of energy density was reported and a modification to the energy density that weighs power more than velocity was proposed that reduced variability. The role of hatch spacing and layer thickness on the LoF porosity was described, and Tang's LoF criterion was validated. The contrasting impact of layer thickness and hatch spacing on the LoF porosity at extreme values was discussed, and the impact of processing parameter on the pore equivalent diameter and sphericity was reported. Four distinct morphological regions were identified that depended on hatch spacing and layer thickness. The quantification and prevention of defects are critical towards enabling the usage of AM parts in structural applications. This methodology enables the relating of processing to final part performance for AM for the purpose of defect avoidance and process optimization and empowers the use of additively manufactured parts.

6. Acknowledgements

The authors gratefully acknowledge the financial support from the National Aeronautics and Space Administration (NASA), Space Technology Research Grants (Early State Innovation Grant No.: 80NSSC20K0294) and the NASA Aeronautics Research Mission Directorate Transformational Tools and Technologies project. The authors thank Samuel J.A. Hocker (NASA Langley Research Center) and Harold D. Claytor (Analytical Mechanics Associates) for providing Figure 1(a). Saikumar R. Yeratapally was sponsored through the NASA Langley Research Center's cooperative agreement 80LARC17C0004 with the National Institute of Aerospace.

References

1. Gong H, Rafi K, Gu H, et al (2014) Analysis of defect generation in Ti–6Al–4V parts made using powder bed fusion additive manufacturing processes. Additive Manufacturing 1–4:87–98. https://doi.org/10.1016/j.addma.2014.08.002

2. Grasso M, Colosimo BM (2017) Process defects and in situ monitoring methods in metal powder bed fusion: a review. Meas Sci Technol 28:044005. https://doi.org/10.1088/1361-6501/aa5c4f

3. Mostafaei A, Zhao C, He Y, et al (2022) Defects and anomalies in powder bed fusion metal additive manufacturing. Current Opinion in Solid State and Materials Science 26:100974. https://doi.org/10.1016/j.cossms.2021.100974

4. Biswal R, Syed AK, Zhang X (2018) Assessment of the effect of isolated porosity defects on the fatigue performance of additive manufactured titanium alloy. Additive Manufacturing 23:433–442. https://doi.org/10.1016/j.addma.2018.08.024

5. Masuo H, Tanaka Y, Morokoshi S, et al (2018) Influence of defects, surface roughness and HIP on the fatigue strength of Ti-6Al-4V manufactured by additive manufacturing. International Journal of Fatigue 117:163–179. https://doi.org/10.1016/j.ijfatigue.2018.07.020

6. Thompson A, Maskery I, Leach R (2016) X-ray computed tomography for additive manufacturing: A review. Measurement Science and Technology 27:072001. https://doi.org/10.1088/0957-0233/27/7/072001

7. du Plessis A, Yadroitsev I, Yadroitsava I, Le Roux SG (2018) X-Ray Microcomputed Tomography in Additive Manufacturing: A Review of the Current Technology and Applications. 3D Printing and Additive Manufacturing 5:227–247. https://doi.org/10.1089/3dp.2018.0060

8. Sola A, Nouri A (2019) Microstructural porosity in additive manufacturing: The formation and detection of pores in metal parts fabricated by powder bed fusion. Journal of Advanced Manufacturing and Processing 1:e10021. https://doi.org/10.1002/amp2.10021

9. Cunningham R, Narra SP, Ozturk T, et al (2016) Evaluating the Effect of Processing Parameters on Porosity in Electron Beam Melted Ti-6Al-4V via Synchrotron X-ray Microtomography. JOM 68:765–771. https://doi.org/10.1007/s11837-015-1802-0

10. Kasperovich G, Haubrich J, Gussone J, Requena G (2016) Correlation between porosity and processing parameters in TiAl6V4 produced by selective laser melting. Materials & Design 105:160–170. https://doi.org/10.1016/j.matdes.2016.05.070

11. Cunningham R, Narra SP, Montgomery C, et al (2017) Synchrotron-Based X-ray Microtomography Characterization of the Effect of Processing Variables on Porosity Formation in Laser Power-Bed Additive Manufacturing of Ti-6Al-4V. JOM 69:479–484. https://doi.org/10.1007/s11837-016-2234-1

12. Neikter M, Forsberg F, Pederson R, et al (2018) Defect characterization of electron beam melted Ti-6Al-4V and Alloy 718 with X-ray microtomography. Aeronautics and Aerospace Open Access Journal 2:139–145

13. Kim FH, Moylan SP, Phan TQ, Garboczi EJ (2020) Investigation of the Effect of Artificial Internal Defects on the Tensile Behavior of Laser Powder Bed Fusion 17–4 Stainless Steel Samples: Simultaneous Tensile Testing and X-Ray Computed Tomography. Exp Mech 60:987–1004. https://doi.org/10.1007/s11340-020-00604-6

14. Brown A, Zachary J, Tilson W (2017) Classification, Effects, and Prevention of Build Defects in Powder-bed Fusion Printed Inconel 718. TMS 2017 Annual Meeting and Exhibition

15. Zhang B, Ham K, Shao S, et al (2017) Effect of Heat Treatment and Hot Isostatic Pressing on the Morphology and Size of Pores in Additive Manufactured Ti-6Al-4V Parts. University of Texas at Austin

16. Du L, Pan X, Qian G, et al (2021) Crack initiation mechanisms under two stress ratios up to very-high-cycle fatigue regime for a selective laser melted Ti-6Al-4V. International Journal of Fatigue 149:106294. https://doi.org/10.1016/j.ijfatigue.2021.106294

17. Cao M, Liu Y, Dunne FPE (2022) A crystal plasticity approach to understand fatigue response with respect to pores in additive manufactured aluminium alloys. International Journal of Fatigue 161:106917. https://doi.org/10.1016/j.ijfatigue.2022.106917

18. Liu QC, Elambasseril J, Sun SJ, et al (2014) The Effect of Manufacturing Defects on the Fatigue Behaviour of Ti-6Al-4V Specimens Fabricated Using Selective Laser Melting. AMR 891–892:1519–1524. https://doi.org/10.4028/www.scientific.net/AMR.891-892.1519

19. Malefane LB, Preez W du, Maringa M, Plessis A du (2018) Tensile and high cycle fatigue properties of annealed Ti6Al4V (ELI) specimens produced by direct metal laser sintering. The South African Journal of Industrial Engineering 29:312–313. https://doi.org/10.7166/29-3-2077

20. Benedetti M, Fontanari V, Bandini M, et al (2018) Low- and high-cycle fatigue resistance of Ti-6Al-4V ELI additively manufactured via selective laser melting: Mean stress and defect sensitivity. International Journal of Fatigue 107:96–109. https://doi.org/10.1016/j.ijfatigue.2017.10.021

21. Beretta S, Romano S (2017) A comparison of fatigue strength sensitivity to defects for materials manufactured by AM or traditional processes. International Journal of Fatigue 94:178–191. https://doi.org/10.1016/j.ijfatigue.2016.06.020

22. Romano S, Beretta S, Miccoli S, Gschweitl M (2020) Probabilistic Framework for Defect Tolerant Fatigue Assessment of Additively Manufactured Parts Applied to a Space Component. In: Structural Integrity of Additive Manufactured Parts. ASTM International, pp 526–539

23. Kabir M, Richter H (2017) Modeling of Processing-Induced Pore Morphology in an Additively-Manufactured Ti-6Al-4V Alloy. Materials 10:145. https://doi.org/10.3390/ma10020145

24. Yeratapally SR, Lang C, Glaessgen EH (2020) A computational study to investigate the effect of defect geometries on the fatigue crack driving forces in powder-bed AM materials. In: AIAA Scitech 2020 Forum. American Institute of Aeronautics and Astronautics, Orlando, FL

25. Tang M, Pistorius PC, Beuth JL (2017) Prediction of lack-of-fusion porosity for powder bed fusion. Additive Manufacturing 14:39–48. https://doi.org/10.1016/j.addma.2016.12.001

26. Mukherjee T, DebRoy T (2018) Mitigation of lack of fusion defects in powder bed fusion additive manufacturing. Journal of Manufacturing Processes 36:442–449. https://doi.org/10.1016/j.jmapro.2018.10.028

27. Promoppatum P, Yao S-C, Pistorius PC, Rollett AD (2017) A Comprehensive Comparison of the Analytical and Numerical Prediction of the Thermal History and Solidification Microstructure of Inconel 718 Products Made by Laser Powder-Bed Fusion. Engineering 3:685–694. https://doi.org/10.1016/J.ENG.2017.05.023

28. Mojumder S, Gan Z, Li Y, et al (2023) Linking process parameters with lack-of-fusion porosity for laser powder bed fusion metal additive manufacturing. Additive Manufacturing 68:103500. https://doi.org/10.1016/j.addma.2023.103500

29. Committee on Integrated Computational Materials Engineering, National Materials Advisory Board, Division of Engineering and Physical Sciences, National Research Council of the National Academies (2008) Integrated Computational Materials Engineering: A Transformational Discipline for Improved Competitiveness and National Security. National Academies Press, Washington

30. Liu PW, Wang Z, Xiao YH, et al (2020) Integration of phase-field model and crystal plasticity for the prediction of process-structure-property relation of additively manufactured metallic materials. International Journal of Plasticity 128:102670. https://doi.org/10.1016/j.ijplas.2020.102670

31. Agius D, O'Toole P, Wallbrink C, et al (2021) Integrating phase field and crystal plasticity finite element models for simulations of titanium alloy Ti-5553. J Phys Mater 4:044014. https://doi.org/10.1088/2515-7639/ac194f

32. Turner JA, Belak J, Barton N, et al (2022) ExaAM: Metal additive manufacturing simulation at the fidelity of the microstructure. The International Journal of High Performance Computing Applications 36:13–39. https://doi.org/10.1177/10943420211042558

33. Irwin J, Reutzel EW, Michaleris P, et al (2016) Predicting Microstructure From Thermal History During Additive Manufacturing for Ti-6Al-4V. Journal of Manufacturing Science and Engineering 138:111007. https://doi.org/10.1115/1.4033525

34. Liu S, Shin YC (2020) Integrated 2D cellular automata-phase field modeling of solidification and microstructure evolution during additive manufacturing of Ti6Al4V. Computational Materials Science 183:109889. https://doi.org/10.1016/j.commatsci.2020.109889

35. Yang X, Barrett RA, Tong M, et al (2020) Prediction of Microstructure Evolution for Additive Manufacturing of Ti-6Al-4V. Procedia Manufacturing 47:1178–1183. https://doi.org/10.1016/j.promfg.2020.04.170

36. Sun W, Shan F, Zong N, et al (2021) Simulation of solidified β grain for Ti–6Al–4V during wire laser additive manufacturing by three-dimensional cellular automaton method. Modelling Simul Mater Sci Eng 29:065006. https://doi.org/10.1088/1361-651X/ac0c23

37. Pham M-S, Dovgyy B, Hooper PA, et al (2020) The role of side-branching in microstructure development in laser powder-bed fusion. Nature Communications 11:749. https://doi.org/10.1038/s41467-020-14453-3

38. Karimi P, Sadeghi E, Ålgårdh J, et al (2021) Tailored grain morphology via a unique melting strategy in electron beam-powder bed fusion. Materials Science and Engineering: A 824:141820. https://doi.org/10.1016/j.msea.2021.141820

39. Liu J, Li G, Sun Q, et al (2022) Understanding the effect of scanning strategies on the microstructure and crystallographic texture of Ti-6Al-4V alloy manufactured by laser powder bed fusion. Journal of Materials Processing Technology 299:117366. https://doi.org/10.1016/j.jmatprotec.2021.117366

40. Popovich VA, Borisov EV, Popovich AA, et al (2017) Functionally graded Inconel 718 processed by additive manufacturing: Crystallographic texture, anisotropy of microstructure and mechanical properties. Materials & Design 114:441–449. https://doi.org/10.1016/j.matdes.2016.10.075

41. Kok Y, Tan XP, Wang P, et al (2018) Anisotropy and heterogeneity of microstructure and mechanical properties in metal additive manufacturing: A critical review. Materials & Design 139:565–586. https://doi.org/10.1016/j.matdes.2017.11.021

42. Balachandramurthi AR, Moverare J, Hansson T, Pederson R (2020) Anisotropic fatigue properties of Alloy 718 manufactured by Electron Beam Powder Bed Fusion. International Journal of Fatigue 141:105898. https://doi.org/10.1016/j.ijfatigue.2020.105898

43. Yan W, Lin S, Kafka OL, et al (2018) Modeling process-structure-property relationships for additive manufacturing. Front Mech Eng 13:482–492. https://doi.org/10.1007/s11465-018-0505-y

44. Kapoor K, Yoo YSJ, Book TA, et al (2018) Incorporating grain-level residual stresses and validating a crystal plasticity model of a two-phase Ti-6Al-4 V alloy produced via additive manufacturing. Journal of the Mechanics and Physics of Solids 121:447–462. https://doi.org/10.1016/j.jmps.2018.07.025

45. Geng Y, Harrison N (2020) Functionally graded bimodal Ti6Al4V fabricated by powder bed fusion additive manufacturing: Crystal plasticity finite element modelling. Materials Science and Engineering: A 773:138736. https://doi.org/10.1016/j.msea.2019.138736

46. Yeratapally SR, Lang CG, Cerrone AR, et al (2022) Effect of defects on the constant-amplitude fatigue behavior of as-built Ti-6Al-4V alloy produced by laser powder bed fusion process: Assessing performance with metallographic analysis and micromechanical simulations. Additive Manufacturing 52:102639. https://doi.org/10.1016/j.addma.2022.102639

47. SPPARKS Kinetic Monte Carlo Simulator. https://spparks.github.io/. Accessed 4 Aug 2022

48. Plimpton S, Battaile C, Chandross M, et al (2009) Crossing the Mesoscale No-Man's Land via Parallel Kinetic Monte Carlo

49. Rodgers TM, Madison JD, Tikare V (2017) Simulation of metal additive manufacturing microstructures using kinetic Monte Carlo. Computational Materials Science 135:78–89. https://doi.org/10.1016/j.commatsci.2017.03.053

50. Rodgers TM, Moser D, Abdeljawad F, et al (2021) Simulation of Powder Bed Metal Additive Manufacturing Microstructures with Coupled Finite Difference-Monte Carlo Method. Additive Manufacturing 101953. https://doi.org/10.1016/j.addma.2021.101953

51. Groeber MA, Jackson MA (2014) DREAM.3D: A Digital Representation Environment for the Analysis of Microstructure in 3D. Integr Mater Manuf Innov 3:56–72. https://doi.org/10.1186/2193-9772-3-5

52. Wadell H (1935) Volume, Shape, and Roundness of Quartz Particles. The Journal of Geology 43:250–280

53. Dilip JJS, Zhang S, Teng C, et al (2017) Influence of processing parameters on the evolution of melt pool, porosity, and microstructures in Ti-6Al-4V alloy parts fabricated by selective laser melting. Prog Addit Manuf 2:157–167. https://doi.org/10.1007/s40964-017-0030-2

54. Schneider CA, Rasband WS, Eliceiri KW (2012) NIH Image to ImageJ: 25 years of image analysis. Nat Methods 9:671–675. https://doi.org/10.1038/nmeth.2089

55. Rosenthal D (1946) The Theory of Moving Sources of Heat and Its Application of Metal Treatments. Transactions of ASME 68:849–866

56. Gordon JV, Narra SP, Cunningham RW, et al (2020) Defect structure process maps for laser powder bed fusion additive manufacturing. Additive Manufacturing 36:101552. https://doi.org/10.1016/j.addma.2020.101552

57. Cepeda-Jiménez CM, Potenza F, Magalini E, et al (2020) Effect of energy density on the microstructure and texture evolution of Ti-6Al-4V manufactured by laser powder bed fusion. Materials Characterization 163:110238. https://doi.org/10.1016/j.matchar.2020.110238

58. King WE, Barth HD, Castillo VM, et al (2014) Observation of keyhole-mode laser melting in laser powder-bed fusion additive manufacturing. Journal of Materials Processing Technology 214:2915–2925. https://doi.org/10.1016/j.jmatprotec.2014.06.005

59. Rubenchik A, Wu S, Mitchell S, et al (2015) Direct measurements of temperature-dependent laser absorptivity of metal powders. Appl Opt 54:7230. https://doi.org/10.1364/AO.54.007230

60. Boley CD, Mitchell SC, Rubenchik AM, Wu SSQ (2016) Metal powder absorptivity: modeling and experiment. Appl Opt 55:6496. https://doi.org/10.1364/AO.55.006496

61. Yeratapally SR, Cerrone A, Tang M, Glaessgen EH (2020) A 3D model to predict explicit morphologies and volume fraction of lack-of-fusion pores generated in selective laser melting processes. NASA/TM–2020-220579.

62. du Plessis A (2019) Effects of process parameters on porosity in laser powder bed fusion revealed by X-ray tomography. Additive Manufacturing 30:100871. https://doi.org/10.1016/j.addma.2019.100871

63. Jolley BR, Uchic MD, Sparkman D, et al (2021) Application of Serial Sectioning to Evaluate the Performance of x-ray Computed Tomography for Quantitative Porosity Measurements in Additively Manufactured Metals. JOM 73:3230–3239. https://doi.org/10.1007/s11837-021-04863-z

64. Brika SE, Letenneur M, Dion CA, Brailovski V (2020) Influence of particle morphology and size distribution on the powder flowability and laser powder bed fusion manufacturability of Ti-6Al-4V alloy. Additive Manufacturing 31:100929. https://doi.org/10.1016/j.addma.2019.100929

65. Montalbano T, Briggs BN, Waterman JL, et al (2021) Uncovering the coupled impact of defect morphology and microstructure on the tensile behavior of Ti-6Al-4V fabricated via laser powder bed fusion. Journal of Materials Processing Technology 294:117113. https://doi.org/10.1016/j.jmatprotec.2021.117113

66. Jin P, Tang Q, Song J, et al (2021) Numerical investigation of the mechanism of interfacial dynamics of the melt pool and defects during laser powder bed fusion. Optics & Laser Technology 143:107289. https://doi.org/10.1016/j.optlastec.2021.107289

67. Caiazzo F, Alfieri V, Casalino G (2020) On the Relevance of Volumetric Energy Density in the Investigation of Inconel 718 Laser Powder Bed Fusion. Materials 13:538. https://doi.org/10.3390/ma13030538

68. Tang M (2017) Inclusions, Porosity, and Fatigue of AlSi10Mg Parts Produced by Selective Laser Melting. Thesis, Carnegie Mellon University

69. Bogdanor MJ, Mahadevan S, Oskay C (2013) Uncertainty quantification in damage modeling of heterogeneous materials. JMC 11:. https://doi.org/10.1615/IntJMultCompEng.2013005821

70. Zhang X, Oskay C (2019) Plastic dissipation sensitivity to mechanical properties in polycrystalline β-HMX subjected to impact loading. Mechanics of Materials 138:103079. https://doi.org/10.1016/j.mechmat.2019.103079

71. Zhang X, Liu Y, Oskay C (2022) Uncertainty Quantification for Microstructure-Sensitive Fatigue Nucleation and Application to Titanium Alloy, Ti6242. Frontiers in Materials 9:

72. Zhang S, Oskay C (2017) Reduced order variational multiscale enrichment method for thermo-mechanical problems. Comput Mech 59:887–907. https://doi.org/10.1007/s00466-017-1380-9

73. Zhang X, Oskay C (2017) Sparse and scalable eigenstrain-based reduced order homogenization models for polycrystal plasticity. Computer Methods in Applied Mechanics and Engineering 326:241–269. https://doi.org/10.1016/j.cma.2017.07.027

74. Zhang X, Liu Y, Oskay C (2022) Multiscale Reduced-Order Modeling of a Titanium Skin Panel Subjected to Thermomechanical Loading. AIAA Journal 60:302–315. https://doi.org/10.2514/1.J060497